

Article

# Molecular Rh(III) and Ir(III) Catalysts Immobilized on Bipyridine-Based Covalent Triazine Frameworks for the Hydrogenation of CO<sub>2</sub> to Formate

Gunniya Hariyanandam Gunasekar <sup>1,2</sup> , Kwangho Park <sup>1</sup>, Hyeonseok Jeong <sup>1</sup> , Kwang-Deog Jung <sup>2</sup>, Kiyoung Park <sup>3</sup> and Sungho Yoon <sup>1,\*</sup>

<sup>1</sup> Department of Applied Chemistry, Kookmin University, 861-1 Jeongneung-dong, Seongbuk-gu, Seoul 136702, Korea; ghguna@gmail.com (G.H.G.); kwangho@kookmin.ac.kr (K.P.); whij2@kookmin.ac.kr (H.J.)

<sup>2</sup> Clean Energy Research Center, Korea Institute of Science and Technology, P.O. Box 131, Cheongryang, Seoul 136-791, Korea; jkdcacat@kist.re.kr

<sup>3</sup> Department of Chemistry, Korea Advanced Institute of Science and Technology, Daejeon 34141, Korea; kiyoung.park@kaist.ac.kr

\* Correspondence: yoon@kookmin.ac.kr

Received: 22 June 2018; Accepted: 20 July 2018; Published: 22 July 2018



**Abstract:** The catalytic reactivity of molecular Rh(III)/Ir(III) catalysts immobilized on two- and three-dimensional Bipyridine-based Covalent Triazine Frameworks (bpy-CTF) for the hydrogenation of CO<sub>2</sub> to formate has been described. The heterogenized Ir complex demonstrated superior catalytic efficiency over its Rh counterpart. The Ir catalyst immobilized on two-dimensional bpy-CTF showed an improved turnover frequency and turnover number compared to its three-dimensional counterpart. The two-dimensional Ir catalyst produced a maximum formate concentration of 1.8 M and maintained its catalytic efficiency over five consecutive runs with an average of 92% in each cycle. The reduced activity after recycling was studied by density functional theory calculations, and a plausible leaching pathway along with a rational catalyst design guidance have been proposed.

**Keywords:** heterogenization on covalent triazine frameworks; immobilized bipyridine complexes; heterogenized Ir and Rh complexes; heterogeneous CO<sub>2</sub> hydrogenation catalyst; leaching pathway of heterogenized half-sandwich complexes

## 1. Introduction

The burgeoning interest of CO<sub>2</sub> as an energy vector for renewable fuel storage and as a C<sub>1</sub> building block for chemical production has renewed attention on CO<sub>2</sub> hydrogenation into formic acid [1–8]. Formic acid and its salts are used as basic chemicals in various industries [9], and are regarded as a liquid form of hydrogen, which is strongly viewed as an ultimate renewable fuel by the scientific and technological community [10]. Thus, formic acid production by CO<sub>2</sub> hydrogenation is one exemplary approach to generate renewable fuels in a fully sustainable carbon-neutral economy.

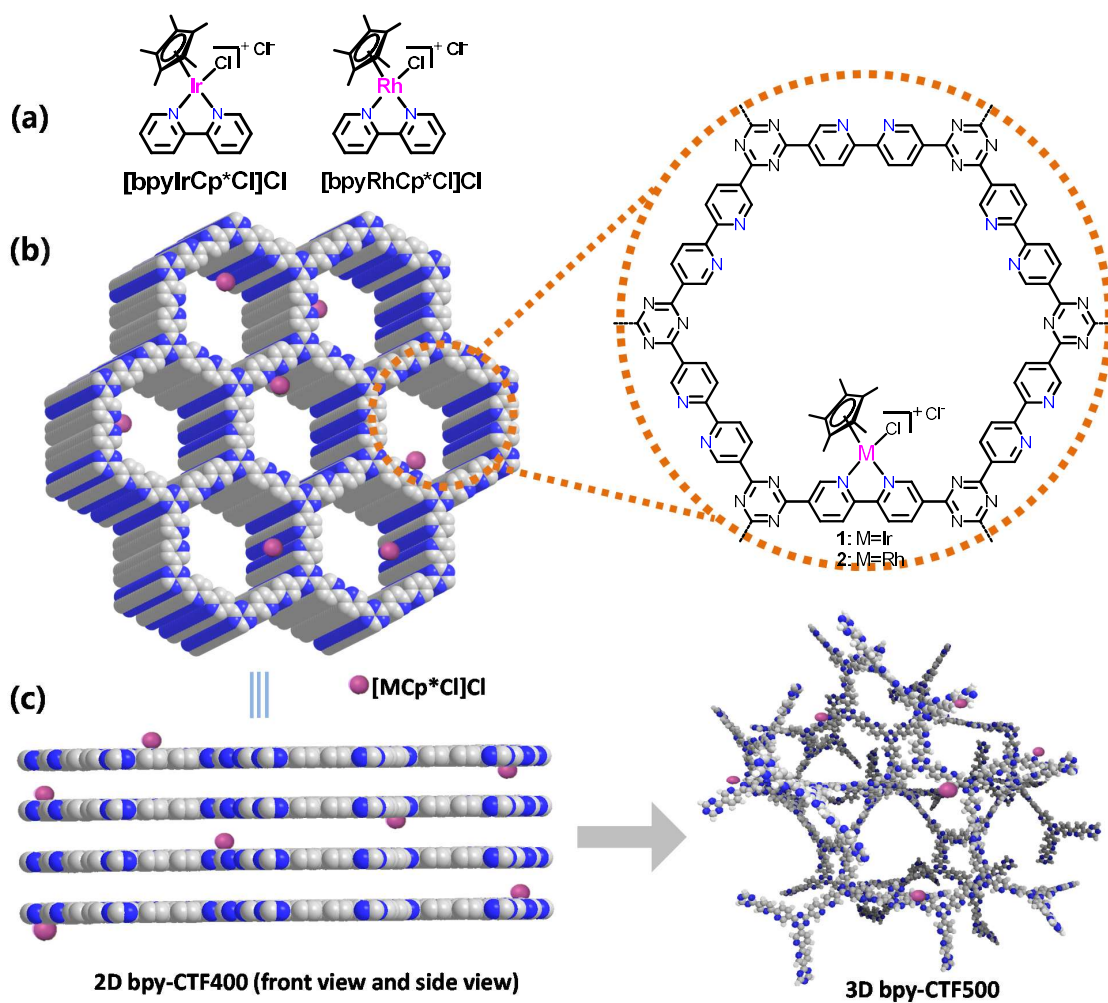
A plethora of homogeneous catalysts has been studied in the hydrogenation of CO<sub>2</sub> into formate/formic acid; of which nitrogen, and phosphine ligated Rh, Ru, and Ir complexes have evolved as effective catalytic systems for this transformation [11–20]. In particular, half-sandwich Rh, Ru, and Ir complexes with bidentate N-donor ligands (2,2'-bipyridine, 1,10-phenanthroline and pyrimidine and its derivatives) have demonstrated excellent catalytic activities and selectivity's in the aqueous phase-catalytic hydrogenation [17–19]. While the reported homogeneous catalysts exhibit excellent activity and selectivity, the challenges encountered for this catalysis are related to the recyclability of catalysts and product isolation (formic acid). The latter is more complicated because the catalysts

also promote formic acid dehydrogenation effectively once the operating pressures are decreased. Therefore, a highly active catalyst that can be easily isolated prior to product separation step with good recyclability is necessary to implement the process in the industries.

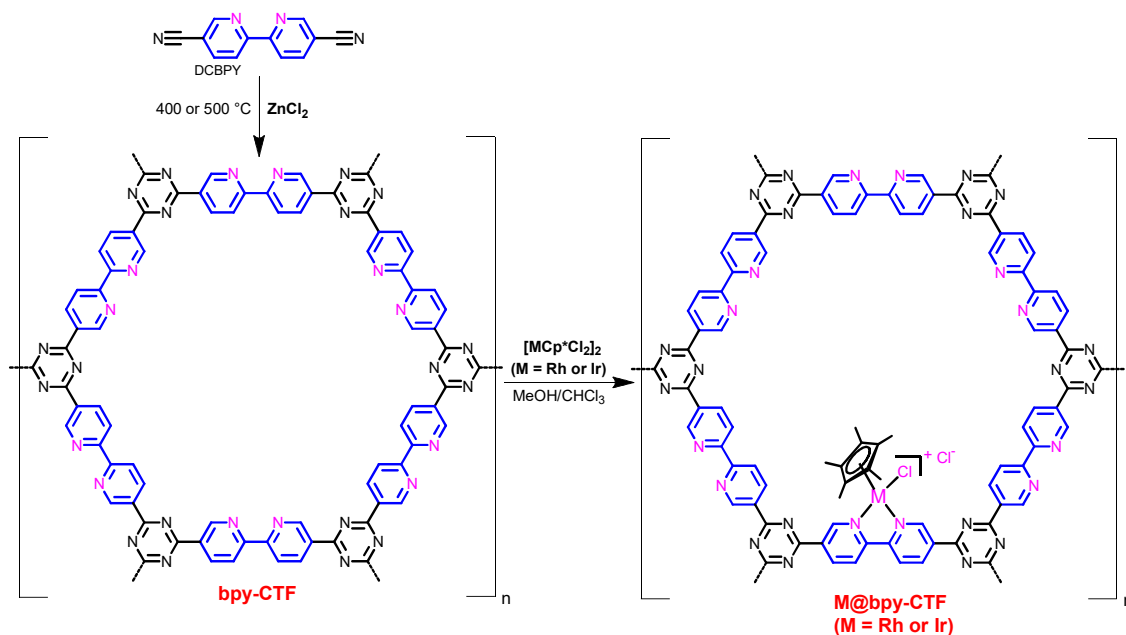
Towards this aim, heterogeneous catalysts have been introduced, owing to their advantages of simple isolation and recyclability [21–45]. A number of heterogeneous metal nanoparticle catalysts that are mainly supported on supports like alumina and TiO<sub>2</sub> have been investigated [33–38,40,42]. In addition, heterogenized catalysts have also been explored, as they combine the classical benefits of homogeneous catalysts (high activity and selectivity) and heterogeneous catalysts (easy isolation and recyclability) [21,26–32,43–45]. In this regard, Ru and Ir complexes supported on conventional supports like silica, MCM-41, polystyrene and polyethyleneimine were examined [24,26,27].

Recently, Covalent Triazine Frameworks (CTFs) have emerged as a novel platform for heterogeneous catalyst supports, owing to their robust and rigid structures, immense thermal and chemical stability, high acid-base resistivity, large surface area, and tunable pore sizes and structures [46–60]. They are usually prepared via trimerization of aromatic nitriles at temperatures above 300 °C using ZnCl<sub>2</sub> as a salt melt [52–56]. CTFs synthesized at different temperatures (300, 400, and 500 °C) usually exhibit different physical and porous (surface) properties; thus, the porous properties of CTFs, which play a key role in heterogeneous catalysis, can be easily tuned by varying the synthesis conditions [54,56,60]. Most interestingly, CTFs with coordinating functional groups in the skeleton have attracted a great deal of attention in the heterogeneous catalysis because they enable anchoring of transition-metal complexes on robust and high-surface-area solid supports [46,58–64]. Consequently, the number of this type of catalyst have increased dramatically in recent years.

Our preliminary results obtained using CTF as a catalyst support for the hydrogenation of CO<sub>2</sub> to formate were reported in our previous communication [29] (Schemes 1b and 2). Therein, the heterogenized Ir catalyst, Ir<sub>4.7</sub>@bpy-CTF400, containing Cp\*-Ir-N\*N(bpy) bonds was demonstrated to be one of the most active surfaces for hydrogenation catalysis. In addition, the Ir catalyst was shown to be recyclable, albeit with slightly reduced activity, for at least five cycles. In the present study, the catalytic efficiency of its Rh counterpart, Rh<sub>1.7</sub>@bpy-CTF400 has been studied (Schemes 1 and 2); the Rh catalyst showed an initial TOF 960 h<sup>-1</sup> in CO<sub>2</sub> hydrogenation. In addition, we investigated whether 2D or 3D CTFs (Scheme 1c) are preferable for the hydrogenation and also influence of the amount of immobilized catalyst on their structures and efficiencies. Using the best catalyst, Ir<sub>4.7</sub>@bpy-CTF400 the effect of base concentration on CO<sub>2</sub> hydrogenation and its impact on the final concentration of formate have been investigated. Finally, reduced activity of the Ir catalyst (Ir<sub>4.7</sub>@bpy-CTF400) at successive runs is studied using density functional theory calculations, and the plausible leaching pathway with future design strategies are proposed.



**Scheme 1.** (a) Structures of the homogeneous complexes. (b) Ideal structures of the catalysts Ir@bpy-CTF400 and Rh@bpy-CTF400. (c) Proposed architectural evolution and structural representation of the catalyst Ir@bpy-CTF500.



**Scheme 2.** A general synthetic scheme for the preparation of bpy-CTF-based Rh and Ir complexes.

## 2. Results and Discussion

### 2.1. Synthesis and Characterization

A general synthetic strategy for the preparation of bpy-CTF-based Rh and Ir complexes has been presented in Scheme 2.

#### 2.1.1. Rh@bpy-CTF400

Following a previously described procedure, bpy-CTF400 was obtained as a black solid through trimerization of 5,5'-dicyano-2,2'-bipyridine (DCBPY, AK Scientific, Inc.) at 400 °C using ZnCl<sub>2</sub> (Sigma Aldrich) salt melt [58]. The synthetic strategy similar to the preparation of Ir<sub>4.7</sub>@bpy-CTF400 has been followed for the synthesis of Rh<sub>1.7</sub>@bpy-CTF400 [29]. In brief, a suspension of bpy-CTF400 in methanol/chloroform mixture was treated with [RhCp\*Cl<sub>2</sub>]<sub>2</sub> at reflux temperature for 24 h under N<sub>2</sub> atmosphere and the resulting black solid was filtered at room temperature and washed thoroughly with methanol and dichloromethane. The obtained black solid, designated as Rh<sub>1.7</sub>@bpy-CTF400, was stable in air and insoluble in most of the common volatile solvents and water.

Scanning electron microscopy (SEM, JEOL LTD, Japan, JEM-7610F operating at an accelerating voltage of 20.0 kV) analysis of complex Rh<sub>1.7</sub>@bpy-CTF400 showed that it has an irregular block shaped morphology, as depicted in Figure 1a. Energy-dispersive spectroscopy (EDS, JEOL LTD, Japan, JEM-7610F operating at an accelerating voltage of 20.0 kV) mapping illustrated the presence of a homogeneous distribution of Rh and Cl atoms throughout the framework (Figure 1b and Figure S1), suggesting the uniform metalation of Rh cations to the bpy units of bpy-CTF400. In addition, the atomic ratio of Rh to Cl was close to the theoretical value of 1:2 (Table S1), indicating the possibility of formation of complex Rh<sub>1.7</sub>@bpy-CTF400 as that of homogeneous [bpyRhCp\*Cl]Cl (the structure is shown in Scheme 1a). Inductively coupled plasma mass spectrometry (ICP-MS, iCAP-Q, Thermo fisher scientific) analysis was performed to determine the exact amount of Rh present in Rh<sub>1.7</sub>@bpy-CTF400, and results revealed 1.72 wt.% (0.167 mmol/g) of Rh was incorporated in Rh<sub>1.7</sub>@bpy-CTF400. Since CTFs synthesized at 400 °C are often considered to be sheet-like 2D ring structures, the 1.72 wt.% of Rh indicates the presence of one {RhCp\*(N-N)Cl<sub>2</sub>} unit in about every ninth CTF ring. N<sub>2</sub> adsorption-desorption analysis (Belsorp II mini, BEL Japan, Inc) was performed at 77 K to reveal the porous properties, and the results are shown in Table S2. Similar to bpy-CTF400,

$\text{Rh}_{1.7}@\text{bpy-CTF400}$  also exists as a microporous material, however the surface area and pore volume decreased from  $684.59 \text{ m}^2/\text{g}$  and  $0.40 \text{ cm}^3/\text{g}$ , as in the original  $\text{bpy-CTF400}$ , to  $151.8 \text{ m}^2/\text{g}$  and  $0.12 \text{ cm}^3/\text{g}$ , respectively. This change indicates that  $\{\text{RhCp}^*\text{Cl}_2\}$  units are partially occupying the pores of the  $\text{bpy-CTF400}$ . Moreover,  $\text{Rh}_{1.7}@\text{bpy-CTF400}$  still presents as a porous material with an average pore diameter of 3.3 nm; thus, small molecules, such as  $\text{CO}_2$ ,  $\text{H}_2$ ,  $\text{H}_2\text{O}$ , and formic acid, can penetrate through its pores easily. To study the exact coordination environment of Rh ions, X-ray photoelectron spectroscopy (XPS, ESCA 2000 (VG microtech) at a pressure of  $\sim 3 \times 10^{-9}$  mbar using Al-K $\alpha$  as the excitation source ( $h\nu = 1486.6 \text{ eV}$ ) was performed and compared with its homogeneous counterpart,  $[\text{bpyRhCp}^*\text{Cl}]\text{Cl}$ ; here, values are referenced to the C1s value of 284.6 eV. As shown in Figure 1c,d, complex  $\text{Rh}_{1.7}@\text{bpy-CTF400}$  and homogeneous  $[\text{bpyRhCp}^*\text{Cl}]\text{Cl}$  show an identical Rh3d $_{5/2}$  EBE value of 309.1 eV, which confirms the similar coordination environments of Rh in both compounds. These results collectively confirm that the formation and coordination environment of the Rh metal center in  $\text{Rh}_{1.7}@\text{bpy-CTF400}$  are similar to those of homogeneous  $[\text{bpyRhCp}^*\text{Cl}]\text{Cl}$ .

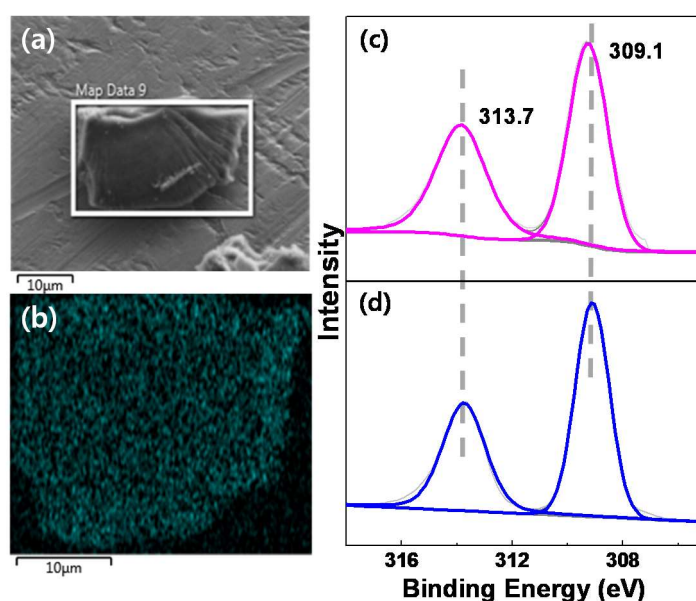


**Figure 1.** (a) SEM image of  $\text{Rh}_{1.7}@\text{bpy-CTF400}$  and (b) the corresponding EDS mapping of Rh. (c,d) Deconvoluted Rh 3d XP spectra of (c)  $\text{Rh}_{1.7}@\text{bpy-CTF400}$  (pink) and (d) homogeneous  $[\text{bpyRhCp}^*\text{Cl}]\text{Cl}$  (blue).

### 2.1.2. Three-Dimensional Architecture of $\text{Ir}@\text{bpy-CTF500}$

Three dimensional  $\text{bpy-CTF}$ , represented as  $\text{bpy-CTF500}$ , was synthesized through the trimerization of DCBPY at  $500 \text{ }^\circ\text{C}$  using  $\text{ZnCl}_2$  as a catalyst as well as a salt melt [58]. The obtained black solid was analyzed by Fourier transform infrared (FT-IR, Nicolet iS 50, Thermo Fisher Scientific) spectroscopy to determine changes in its functional groups during the trimerization at  $500 \text{ }^\circ\text{C}$ , and results were compared with those of  $\text{bpy-CTF400}$ . As shown in Figure 2a, a number of well-resolved and sharp bands of  $\text{bpy-CTF400}$  have disappeared in  $\text{bpy-CTF500}$  and the overall IR bands were very broad and weak. This indicates that the carbonization/rearrangement reaction, i.e., cross-linking between the aromatic groups of stacked layers, has occurred. Elemental analysis showed that carbon content is increased in  $\text{bpy-CTF500}$  compared to  $\text{bpy-CTF400}$  (Table S3). These results demonstrate that the scaffolded covalent structure of  $\text{bpy-CTF500}$  changed significantly from  $\text{bpy-CTF400}$  into a characteristic graphenel polymer. Moreover, the presence of three types of N 1s configurations, corresponding to pyridinic nitrogen ( $\text{N}_i$ ) at 398.2 eV, pyrrolic nitrogen ( $\text{N}_{ii}$ ) at 399.5 eV, and quaternary nitrogen ( $\text{N}_{iii}$ ) at 400.8 eV (Figure 2b) [47], in the XPS analysis of  $\text{bpy-CTF500}$  strongly confirm the occurrence of a cross-linking/rearrangement reaction between the aromatic groups of the stacked

layers; this finding supports the observation that the structure of the catalyst had evolved into a typical graphitized polymer. Besides these chemical structural changes, cross-linking reactions between the aromatic groups of 2D stacked layers can cause evolution of the pore structures in bpy-CTF500. To describe the pore evolution of bpy-CYF500, the  $N_2$  adsorption-desorption results of this material were compared with those of bpy-CTF400 (Figure 2c). The  $N_2$  adsorption-desorption curve of bpy-CTF400 follows a typical type I isotherm, thus indicating that it is a microporous material. By contrast, the  $N_2$  adsorption-desorption curve of bpy-CTF500 showed a sharp uptake in the low-pressure region, a round knee with a hysteresis loop, and an increased uptake at higher relative pressures; these characteristics indicate the generation of new mesopores in addition to a large amount of micropores. As mentioned above, the surface area and pore volume of bpy-CTF500 dramatically increased to  $1566 \text{ m}^2/\text{g}$  and  $0.87 \text{ cm}^3/\text{g}$ , respectively, or nearly twofold those of bpy-CTF400 (Table S2). Considering findings in previous research [47], all of our characterizations thus far collectively confirm that the 2D sheet-like structure of bpy-CTF400 successfully evolves into a 3D architecture at elevated trimerization temperature via cross-linking reactions between the aromatic groups of the stacked layers.

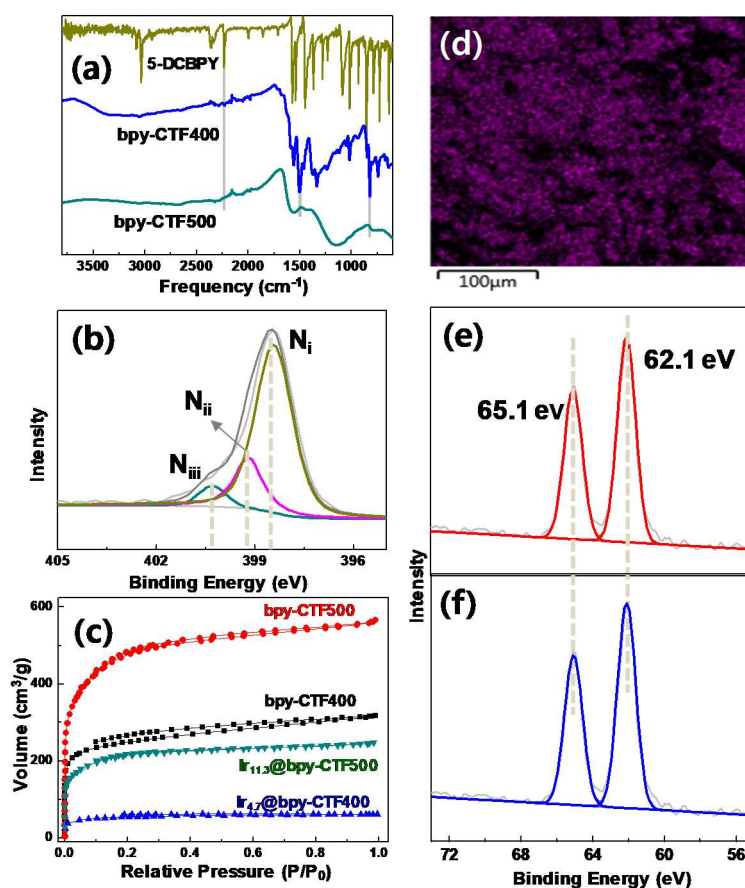


**Figure 2.** Structural characterization of bpy-CTF500 and Ir<sub>11.3</sub>@bpy-CTF500. (a) FT-IR spectra of bpy-CTFs. (b) XPS of N 1s deconvolution spectrum of bpy-CTF500. (c)  $N_2$  adsorption-desorption isotherm. (d) SEM-EDS Ir mapping of Ir<sub>11.3</sub>@bpy-CTF500. Deconvoluted Ir 4f XP spectra of (e) Ir<sub>11.3</sub>@bpy-CTF500 (red) and (f) homogeneous [bpyIrCp\*Cl]Cl (blue).

The successfully synthesized 3D bpy-CTF500 was subsequently metalated with [IrCp\*Cl<sub>2</sub>]<sub>2</sub> following a previously described method, and Ir<sub>11.3</sub>@bpy-CTF500 was obtained without any changes to the color of the original bpy-CTF. The uniform metalation of Ir cation and the 1:2 atomic ratios of Ir to Cl atoms in Ir<sub>11.3</sub>@bpy-CTF500 was confirmed by SEM-EDS analysis (Figures 2d and S2, and Table S1). While the amount of [IrCp\*Cl<sub>2</sub>]<sub>2</sub> treated with bpy-CTF500 was identical to that treated

with bpy-CTF400, ICP-MS analysis of Ir<sub>11.3</sub>@bpy-CTF500 revealed that a very large amount of Ir, at 11.3 wt.% (0.587 mmol/g), was incorporated into Ir<sub>11.3</sub>@bpy-CTF500, corresponding to ~33% total bpy units bound to the Ir(III) center. This finding may be attributed to the large pore volume of 3D bpy-CTF500. N<sub>2</sub> adsorption-desorption analysis demonstrated that the porous characteristic of bpy-CTF500 was maintained in Ir<sub>11.3</sub>@bpy-CTF500, although about twofold decrements in surface area and pore volume compared with those of the original bpy-CTF500 were observed (Figure 2c and Table S2). This result indicates that the pores of bpy-CTF500 are partially occupied by the {[IrCp\*Cl]Cl} unit. XPS analysis of Ir<sub>11.3</sub>@bpy-CTF500 illustrated that the EBE value of Ir4f<sub>7/2</sub> is 62.1 eV, matching that of homogeneous [bpyIrCp\*Cl]Cl exactly (Figure 2e,f) [29]. These results collectively reveal the successful formation of the 3D complex Ir<sub>11.3</sub>@bpy-CTF500 and indicate that both CTFs (bpy-CTF400 and bpy-CTF500) afford the exact same coordination environment of Ir regardless of the architecture of the bpy-CTF.

### 2.1.3. Ir@bpy-CTF400 with Various Ir Loadings

Ir@bpy-CTF400 with different Ir loading amounts were synthesized by treating bpy-CTF400 (0.15 g) with varied amounts of [IrCp\*Cl<sub>2</sub>]<sub>2</sub> (0.03, 0.07 and 1.00 g). Thus, besides Ir<sub>4.7</sub>@bpy-CTF400 where Ir content was 4.7 wt.%, three catalysts with Ir contents of 1.4, 4.1, and 10.6 wt.% were obtained (determined by ICP-MS) and denoted as Ir<sub>1.4</sub>@bpy-CTF400, Ir<sub>4.1</sub>@bpy-CTF400, and Ir<sub>10.6</sub>@bpy-CTF400, respectively. N<sub>2</sub> sorption measurements demonstrated that the pore volume and surface area of Ir<sub>1.4</sub>@bpy-CTF400, Ir<sub>4.1</sub>@bpy-CTF400, and Ir<sub>10.6</sub>@bpy-CTF400 were 0.28, 0.30, and 0.01 cm<sup>3</sup>/g and 479.9, 257.4, and 9.74 m<sup>2</sup>/g, respectively (Table S2); these results were consistent with the metal loading amount, and since Ir<sub>10.6</sub>@bpy-CTF400 contains higher metal loading, it had shown a very small pore volume and surface area. EDS analysis revealed that the atomic ratios of Ir to Cl in Ir<sub>1.4</sub>@bpy-CTF400 and Ir<sub>4.1</sub>@bpy-CTF400, were close to the theoretical value (1:2), similar to Ir<sub>4.7</sub>@bpy-CTF400, but that of Ir<sub>10.6</sub>@bpy-CTF400 was slightly lower (1:1.6) (Table S1). XPS measurements of Ir<sub>1.4</sub>@bpy-CTF400, Ir<sub>4.1</sub>@bpy-CTF400, and Ir<sub>10.6</sub>@bpy-CTF400 further revealed that all of the materials presented an Ir4f<sub>7/2</sub> EBE value of 62.1 eV (Figure 3) [29], which was attributed to the coordination of Ir cations with the bpy unit of bpy-CTF. However, Ir<sub>10.6</sub>@bpy-CTF400 showed a second more-reduced Ir species at 60.9 eV (Figure 3d), which correspond to the Ir(0) species [27]. The formation of reduced Ir species in Ir<sub>10.6</sub>@bpy-CTF400 is likely corroborated by the porous property of bpy-CTF400, as discussed below. Table S2 (entries 1, 3, 6–8) clearly demonstrates that when the Ir content in Ir@bpy-CTF400 is 4.7 wt.%, the pore volume is reduced by about 4 times (0.09 cm<sup>3</sup>/g) in comparison with that of the original bpy-CTF400 (0.40 cm<sup>3</sup>/g). When bpy-CTF400 is treated with an excess of the Ir precursor, most of the bpy-CTF400 pores are initially occupied (up to 4.7 wt.%) by {IrCp\*Cl<sub>2</sub>} units through the formation of an Ir(III) complex and only fewer pores are then available to accommodate excess {IrCp\*Cl<sub>2</sub>} units, and so coordination between the remaining Ir cations and the bpy units of bpy-CTF400 cannot progress. Consequently, Ir(0) species may be generated through the abundant availability of nitrogen sites present in bpy-CTF400 acting as initial nucleation sites. Notably, nucleation sites of substitutional nitrogen species for the formation of nanoparticles has been documented in N-doped carbon materials [65]. Similarly, the formation of Pt(0) and Pd(0) nanoparticles precursors has been observed previously when bpy-CTF was treated with Pt(II) and Pd(II) precursors [58]. These results collectively reveal that the successful formation of Ir@bpy-CTF400 complex structure is closely related to the porosity of the CTF.

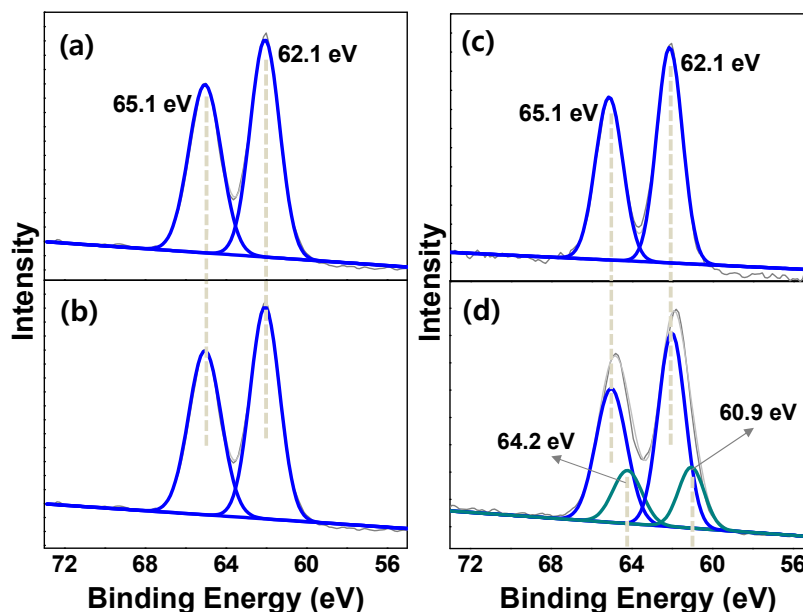


**Figure 3.** Ir 4f XP spectra of (a) Ir<sub>1.4</sub>@bpy-CTF400, (b) Ir<sub>4.1</sub>@bpy-CTF400, (c) Ir<sub>4.7</sub>@bpy-CTF400 and (d) Ir<sub>10.6</sub>@bpy-CTF400 (the peaks corresponding to the binding energy of Ir(III) complex is represented using blue and the peaks corresponding to the binding energy of Ir(0) species is represented using green).

## 2.2. Hydrogenation of CO<sub>2</sub> into Formate

### 2.2.1. Effect of Rh and Ir Metal Centers

Half-sandwich Ru, Rh, and Ir complexes with bidentate N-donor ligands (e.g., bpy, 1,10-phenanthroline, pyrimidine, and their derivatives) exhibit excellent catalytic activity toward CO<sub>2</sub> hydrogenation to formate in aqueous media [17–19]. Although these catalysts feature the same backbone, significant differences in catalytic activity was observed when a different metal center is employed within the same array of ligands [17]. Among the metal-centered Ru, Rh, and Ir complexes with the same ligand groups, Ir complexes exhibit the highest activity [18]. However, in the case of unsubstituted bpy and 1,10-phenanthroline ligated Ru, Rh, and Ir complexes, Rh metal-centered complexes demonstrated better activity [17]. These findings encouraged us to tailor the structural design of Rh<sub>1.7</sub>@bpy-CTF400 and validate the observed metal-center behavior in heterogenized catalysts.

In our previous communication, we observed the optimal catalytic activity of Ir<sub>4.7</sub>@bpy-CTF400 at 8 MPa total pressure (CO<sub>2</sub>/H<sub>2</sub> = 1) in 1 M triethylamine (Et<sub>3</sub>N) solution [29]. Therefore, the catalytic performance of Rh<sub>1.7</sub>@bpy-CTF400 was examined in 1 M Et<sub>3</sub>N solution under 8 MPa total pressure and the results are summarized in Table 1. As shown in Table 1, entry 1, the Rh catalyst produces a formate concentration of 0.01 M in 2 h at 80 °C with turnover number (TON) of 168. The catalyst demonstrated a maximum TON of 1410 with an initial TOF of 960 h<sup>-1</sup> at 120 °C under 8 MPa total pressure and generated a maximum formate concentration of 0.11 M (Table 1, entries 1–4). By comparison, Ir<sub>1.4</sub>@bpy-CTF400 exhibited a TON of 5000 in 2 h and afforded a maximum formate concentration of 0.60 M under the same reaction conditions (Table 1, entry 5). To investigate the recyclability of Rh<sub>1.7</sub>@bpy-CTF400, the solid obtained after each run was recovered by filtration, washed with water and acetone, dried at 80 °C under vacuum for 8 h, and reused for next cycle. As shown as entries 6 and 7 in Table 1, after each run ca. 80% of the catalytic activity was maintained. These results clearly indicate that the catalytic efficiency of Ir<sub>4.7</sub>@bpy-CTF400 is superior to that of Rh<sub>1.7</sub>@bpy-CTF400, in contrast to the trend of the homogeneous catalysts. On the basis of these findings, the Ir metal-centered catalysis were subjected to further studies.

**Table 1.** Catalytic Performances of Rh<sub>1.7</sub>@bpy-CTF400 in comparison with Ir<sub>1.4</sub>@bpy-CTF400 <sup>a</sup>.

Entry	Catalyst	T (°C)	Final Formate Concentration (M)	TON <sup>b</sup>	TOF <sup>c</sup> (h <sup>-1</sup> )
1	Rh <sub>1.7</sub> @bpy-CTF400	80	0.01	168	84
2	Rh <sub>1.7</sub> @bpy-CTF400	100	0.03	440	220
3	Rh <sub>1.7</sub> @bpy-CTF400	120	0.11	1410	705
4	Rh <sub>1.7</sub> @bpy-CTF400	120	0.02	240	960
5	Ir <sub>1.4</sub> @bpy-CTF400	120	0.60	5000	2500
6 <sup>d</sup>	Rh <sub>1.7</sub> @bpy-CTF400	80	0.01	78	39
7 <sup>e</sup>	Rh <sub>1.7</sub> @bpy-CTF400	80	<0.01	57	29

<sup>a</sup> The hydrogenation of CO<sub>2</sub> was carried out in 1 M aqueous Et<sub>3</sub>N solution (20.0 mL) under 8 MPa total pressures (CO<sub>2</sub>/H<sub>2</sub> = 1) for 2 h using [Rh] or [Ir] = 0.122 mM. <sup>b</sup> TON = concentration of formate/concentration of Ir.

<sup>c</sup> TOF = TON h<sup>-1</sup>. <sup>d</sup> Second recycle. <sup>e</sup> Third recycle.

### 2.2.2. Influence of Three-Dimensional Architecture of Ir@bpy-CTF500

The structure of CTFs synthesized at 400 °C is usually believed to be restricted to 2D sheets stacked together via van der Waals forces; these frameworks commonly exhibit a laminar architecture with periodic pore structures [66]. Very recently, structural evolution of the 2D structure of CTFs into a 3D architecture via cross-linking reactions between the stacked sheets was explored using m-CTF by synthesizing the CTF at temperatures exceeding 400 °C [47]. m-CTF and other CTF synthesized above 400 °C displayed a dramatic increase in surface area and pore volume [47,53,56]. Hence, we envisaged that if 3D bpy-CTF is employed as a catalyst support, the resulting heterogenized Ir catalyst would also feature a 3D architecture with a large pore volume and surface area. Thus, bpy-CTF synthesized at 500 °C (designated as bpy-CTF500) was employed as catalyst support to heterogenize the Ir complex (Scheme 1c). Surprisingly, to date, the catalytic properties of heterogenized 3D CTF-based complexes, and the comparative studies between 2D and 3D CTFs within the same array of monomers have not yet been demonstrated.

To check the catalytic performance of Ir<sub>11.3</sub>@bpy-CTF500, CO<sub>2</sub> hydrogenation was performed in 1 M aqueous Et<sub>3</sub>N solution at 120 °C under 8 MPa total pressure, and the results are compared with those of Ir<sub>4.7</sub>@bpy-CTF400 in Table 2, entries 1–3. As expected, Ir<sub>11.3</sub>@bpy-CTF500 also catalyzed the hydrogenation of CO<sub>2</sub> to formate and generated 0.26 M formate in 2 h with an initial TOF of 2480 h<sup>-1</sup> and TON of 2720, which are about twofold lesser than Ir<sub>4.7</sub>@bpy-CTF400. However, as the reaction duration was increased, formate generation by Ir<sub>11.3</sub>@bpy-CTF500 also gradually increased and reached 0.6 M after 6 h. While the XPS results of Ir<sub>4.7</sub>@bpy-CTF400 and Ir<sub>11.3</sub>@bpy-CTF500 at the Ir4f<sub>7/2</sub> level were not very different, the activity of Ir<sub>11.3</sub>@bpy-CTF500 was significantly lower than that of Ir<sub>4.7</sub>@bpy-CTF400. We envisage that Ir<sub>4.7</sub>@bpy-CTF400 possesses relatively more hydrophilic character than Ir<sub>11.3</sub>@bpy-CTF500 and thus, diffusion of the reactants (CO<sub>2</sub>, H<sub>2</sub>, H<sub>2</sub>O, and Et<sub>3</sub>N) and product (triethylammonium formate) occurs more smoothly in Ir<sub>4.7</sub>@bpy-CTF400 than in Ir<sub>11.3</sub>@bpy-CTF500, leading to the faster generation of formate. Further studies are necessary to clarify the micro-level arrangements of bpy units as well as Ir active centers on the pore surfaces of Ir<sub>4.7</sub>@bpy-CTF400 and Ir<sub>11.3</sub>@bpy-CTF500. Thus, the 2D sheet-like structure of bpy-CTF is more advantageous than its 3D structure in obtaining heterogenized Ir(III) complex with optimal catalytic performance for the hydrogenation of CO<sub>2</sub>.

**Table 2.** Catalytic Performances of catalysts Ir<sub>11.3</sub>@bpy-CTF500, Ir<sub>1.4</sub>@bpy-CTF400, Ir<sub>4.1</sub>@bpy-CTF400, and Ir<sub>10.6</sub>@bpy-CTF400 in comparison with Ir<sub>4.7</sub>@bpy-CTF400 <sup>a</sup>.

Entry	Catalyst	Final Formate Concentration (M)	TON <sup>b</sup>	TOF (h <sup>-1</sup> ) <sup>c</sup>
1 <sup>d</sup>	Ir <sub>4.7</sub> @bpy-CTF400	0.60	5000	2500
2	Ir <sub>11.3</sub> @bpy-CTF500	0.26	2720	1360
3 <sup>e</sup>	Ir <sub>11.3</sub> @bpy-CTF500	0.60	5000	2480 <sup>f</sup>
4	Ir <sub>1.4</sub> @bpy-CTF400	0.60	5000	2500
5	Ir <sub>4.1</sub> @bpy-CTF400	0.60	5000	2500
6	Ir <sub>10.6</sub> @bpy-CTF400	0.37	3032	1516

<sup>a</sup> The hydrogenation of CO<sub>2</sub> was carried out in 1 M aqueous Et<sub>3</sub>N solution (20.0 mL) at 120 °C under 8 MPa total pressures (CO<sub>2</sub>/H<sub>2</sub> = 1) for 2 h using [Ir] = 0.122 mM. <sup>b</sup> TON = concentration of formate/concentration of Ir.

<sup>c</sup> TOF = TON h<sup>-1</sup>. <sup>d</sup> See Ref 28. <sup>e</sup> Time = 6 h. <sup>f</sup> Initial TOF for 15 min.

### 2.2.3. Effect of Ir Loadings on Ir@bpy-CTF400

The presence of abundant bpy sites in the bpy-CTF could possibly lead to heterogenization of a large amount of metal complexes on bpy-CTF; thereby the resulting catalyst could have an increased number of active sites per gram of support. As discussed earlier, besides Ir loading of 4.7 wt.% (Ir<sub>4.7</sub>@bpy-CTF400), loadings of 1.4, 4.1 and 10.6 wt.% Ir were synthesized. CO<sub>2</sub> hydrogenation to formate using Ir<sub>1.4</sub>@bpy-CTF400, Ir<sub>4.1</sub>@bpy-CTF400 and Ir<sub>10.6</sub>@bpy-CTF400 was performed under an Ir concentration of 0.122 mM at 120 °C and 8 MPa total pressure in 1 M aqueous Et<sub>3</sub>N solution for 2 h; the results of these experiments are summarized in Table 2 (entries 1, 4–6). Both Ir<sub>1.4</sub>@bpy-CTF400 and Ir<sub>4.1</sub>@bpy-CTF400 generated a formate concentration of 0.6 M with TON of 5000 within 2 h, thereby indicating that they are as active as Ir<sub>4.7</sub>@bpy-CTF400. By contrast, Ir<sub>10.6</sub>@bpy-CTF400 generated only 0.370 M formate with TON of 3032 within 2 h; this concentration is about 1.6 times less than that produced by Ir<sub>4.7</sub>@bpy-CTF400. The reduced activity of Ir<sub>10.6</sub>@bpy-CTF400 may be attributed to the presence of either reduced Ir species or multinuclear Ir metal centers. Similar results were previously observed by Hicks et al. during polyethyleneimine-tethered iminophosphine/Ir-catalyzed CO<sub>2</sub> hydrogenation [27]. Therefore, the better activity of Ir@bpy-CTF400 was maintained until an Ir loading of 4.7 wt.% was achieved, after which it decreased as the catalyst loading continued to increase to 10.6 wt.%, indicating the Ir catalyst loading amount on bpy-CTF400 must be tuned to achieve the optimal performance of Ir@bpy-CTF400.

### 2.2.4. Effect of Base Concentrations on the Production of Formate

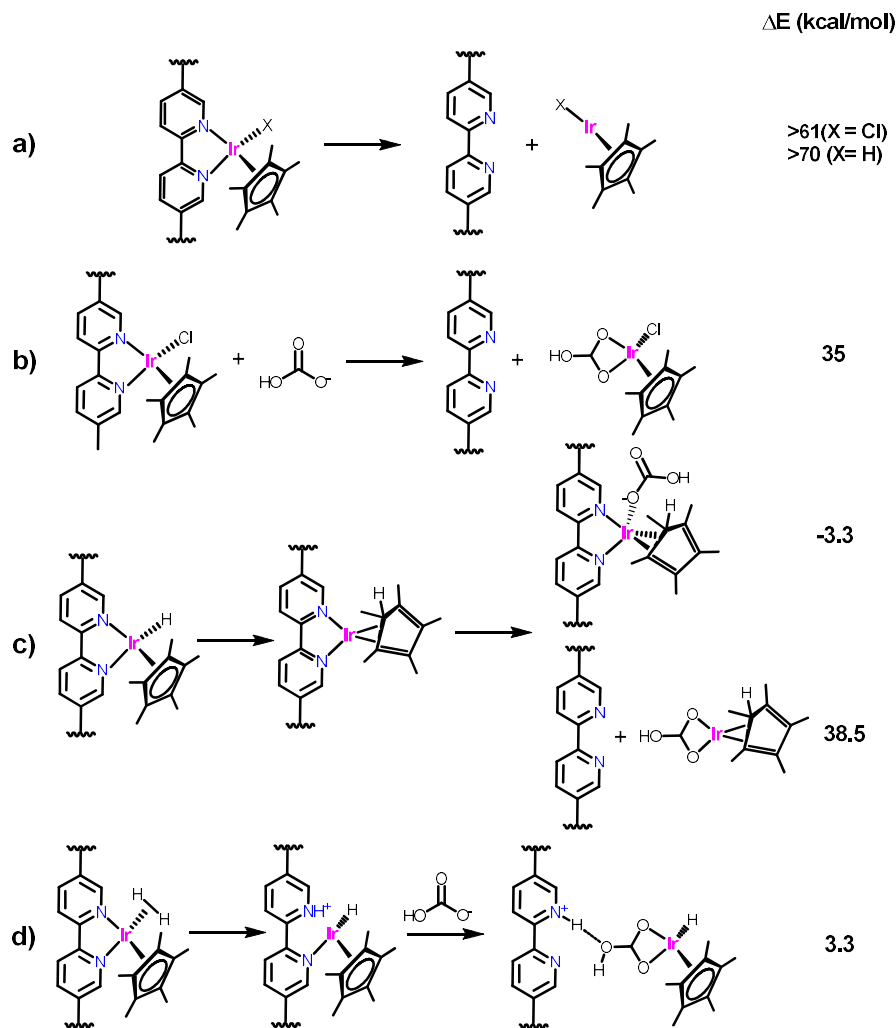
To employ CO<sub>2</sub> hydrogenation catalysts industrially, apart from high TOF (TON), the catalyst must generate high formate concentrations within a short reaction time. Thus, we aimed to increase the formate concentration generated by catalyst Ir<sub>4.7</sub>@bpy-CTF400. Based on the available reports and our experience, CO<sub>2</sub> hydrogenation reaches chemical equilibrium during the conversion and restricts further generation of formate [67]. Hence, the concentration of formate produced by Ir<sub>4.7</sub>@bpy-CTF400 at 120 °C under 8 MPa total pressure in 1 M Et<sub>3</sub>N solution was limited to ~0.6 M even after 10 h. Therefore, to shift the chemical equilibrium toward the product side, hydrogenation was performed in solutions with various concentrations of Et<sub>3</sub>N using Ir<sub>4.7</sub>@bpy-CTF400 (0.12 mM) at 120 °C under 8.0 MPa total pressure. As shown in Table S4, when the concentration of Et<sub>3</sub>N was increased to 2 M, formate generation increased to 0.79 M in 2 h and reached equilibrium (1.18 M) after 7 h. Similarly, in 3 M aqueous Et<sub>3</sub>N solution, formate concentrations of 0.84 and 1.34 M were obtained within 2 and 5 h, respectively; in this system, equilibrium, with 1.80 M formate produced, was achieved after 10 h. This result clearly indicates that the production of formate with high concentration is limited (up to 1.80 M) in the aqueous phase CO<sub>2</sub> hydrogenation catalysis. Finally, to generate this high formate concentration at a relatively short reaction time, the catalyst concentration was increased to 1.22 mM and obtained 1.80 M of formate within 4 h.

### 2.2.5. Leaching and Computational Studies

Although the recycling performance of Ir<sub>4.7</sub>@bpy-CTF400 is better than that of Rh<sub>1.7</sub>@bpy-CTF400 (Figure S6), the efficiency of Ir<sub>4.7</sub>@bpy-CTF400 in successive runs also decreases, with approximately 92% of the activity being retained for each cycle [29]. To investigate this, the resulting filtrate and precipitate were analyzed using ICP-AES and XPS, respectively. ICP-AES analysis revealed that the Ir content in the precipitate decreased to 4.38 wt.% from the original content of 4.7 wt.% (about 6.8% was decreased). Analysis of the filtrate showed that it contained approximately 7.1 ppm Ir, indicating that 5.5% of the originally loaded Ir is leached. XPS analysis of the precipitate showed that no changes in the binding energies of Ir occur (Figure S7); this suggests that the coordination environment of heterogenized Ir(III) catalyst remains unchanged upon use. These results clearly suggest that the reduced activity of Ir<sub>4.7</sub>@bpy-CTF400 in successive runs mainly originates from Ir leaching.

To obtain insight into the pathway(s) of catalyst leaching, density functional theory (DFT) calculations were performed (Scheme 3). As shown in Scheme 3a, the dissociation of bpy from the metal center at the resting state catalysts is highly endergonic ( $\geq 61$  kcal/mol); thus, the possibility of direct dissociation of {IrCp\*Cl} or {IrCp\*H} unit is excluded. Recently, Crabtree et al. showed through computational studies that the half-sandwich Ir precursor [IrCp\*Cl<sub>2</sub>]<sub>2</sub> undergoes decomposition in the presence of carbonate salts and forms a carbonate bound IrCp\*Cl species [68,69]. Based on this, other possible routes were proposed. Owing to the high CO<sub>2</sub> pressure and the use of basic aqueous media in CO<sub>2</sub> hydrogenation, the bicarbonate (HCO<sub>3</sub><sup>-</sup>) is present to a significant extent in the reaction. Thus, we anticipate that HCO<sub>3</sub><sup>-</sup> could react with Ir centers and displace the bpy unit. However, theoretical calculations revealed that the replacement of bpy with HCO<sub>3</sub><sup>-</sup> is also highly endergonic (35 kcal/mol) (Scheme 3b). The dissociation of bpy from a reduced monovalent metal center obtained via hydride transfer to the Cp\*-ring is also endergonic (38.5 kcal/mol) (Scheme 3c). The theoretical calculations performed by Himeda et al. showed that the heterolysis of H<sub>2</sub> occurs via the transfer of a proton to HCO<sub>3</sub><sup>-</sup> [70,71]. Considering these calculations, we anticipate that the heterolysis of H<sub>2</sub> occurs as a minor pathway via proton transfer to the bpy N-site (Scheme 3) since the bpy N is always vicinal to the metal center and the incoming H<sub>2</sub> molecule (i.e., the bulky Cp\* pushes bpy and other ligands to one side). Subsequently, the bond between the Ir and bpy could dissociate and allow the Ir species to leach into the solution. DFT calculation for this pathway suggested that the heterolysis of H<sub>2</sub> via proton transfer to the bpy N-site is feasible with  $\Delta E \sim 14.1$  kcal/mol and further reaction with HCO<sub>3</sub><sup>-</sup> stabilizes the Ir center, allowing the dissociation of bpy-site from the metal center with the overall thermodynamics of  $\Delta E \sim 3.3$  kcal/mol (Scheme 3d). The energy barrier for the process was calculated to be 23.7 kcal/mol, which is reasonable for the reaction temperature used (120 °C).

Thus, the dissociation of Ir-N bond through the proton transfer to bpy N-site during H<sub>2</sub> heterolysis is most presumably responsible for the low recyclability of Ir catalyst. These results propose that a different Ir-surface bond instead of {Cp\*-Ir-N^N} is required to achieve a good recyclability of hydrogenation catalysts. With this understanding, we suggest twofold design strategies for the effective Ir catalyzed hydrogenation of CO<sub>2</sub>: (1) Employing tridentate pincer type (such as N^N^N) frameworks instead of bidentate bpy-CTF. (2) Replacing Cp\* in the {Cp\*-Ir-N^N} surface with ligand(s) that rapidly abstract the proton from H<sub>2</sub> heterolysis such as oxyanionic ligands (acetylacetonate, carboxylate, and carbonate); these ligands could inhibit the deleterious interaction between bpy N-site with H<sub>2</sub> via changing the coordination mode from bidentate to monodentate.



Scheme 3. Plausible leaching pathways of the heterogenized Ir catalyst.

### 3. Conclusions

Heterogenized half-sandwich Rh(III) and Ir(III)-bipyridine complexes were synthesized through post-synthetic metalation of bpy-CTF with Rh/Ir precursor using coordination bonding. The influence of central metal cation in the hydrogenation clearly pictured that the Rh complex is less efficient compared to the Ir complex. The 3D bpy-CTF, synthesized through structural evolution of the 2D bpy-CTF, was employed as a catalyst support for synthesizing 3D heterogenized Ir(III) catalyst. Studies using the different architectural structures of CTFs revealed that the CTFs architectures significantly affect the efficiency of catalysts; the 2D Ir catalyst demonstrated higher efficiency in the hydrogenation of CO<sub>2</sub> compared to 3D catalyst. Metal loading studies on 2D bpy-CTF revealed that there is a critical balance between the CTF porosity and amount of Ir(III) complex to maintain the desired Cp\*-Ir-N<sup>+</sup>N complex structure; Ir loading of up to 4.7 wt.% is optimal for the formation of heterogenized Ir@bpy-CTF400 catalyst with maximal catalytic activity. Studies on the hydrogenation of CO<sub>2</sub> in solutions with various concentrations of Et<sub>3</sub>N unveiled that the generation of high formate concentration is limited; in a solution of 3 M Et<sub>3</sub>N at 120 °C under 8 MPa pressure produced a maximum formate concentration of 1.8 M. Although the Ir catalyst is easily separable and efficient, the activity upon recycling was reduced; leaching studies indicated that about 5.5% of the originally loaded Ir has been leached into the solution. DFT calculations on the leaching pathway showed that interaction between bpy N-site and H<sub>2</sub> during heterolysis of H<sub>2</sub> is the basis for Ir-N bond dissociation.

Based on this understanding, twofold design strategies were suggested to develop recyclable and efficient heterogeneous catalytic systems.

**Supplementary Materials:** The following are available online at <http://www.mdpi.com/2073-4344/8/7/295/s1>, Figure S1: SEM-EDS mapping of catalyst Rh<sub>1.7</sub>@bpy-CTF400. Figure S2: SEM-EDS mapping of catalyst Ir<sub>11.3</sub>@bpy-CTF500. Figure S3: SEM-EDS mapping of catalyst Ir<sub>1.4</sub>@bpy-CTF400. Figure S4: SEM-EDS mapping of catalyst Ir<sub>4.1</sub>@bpy-CTF400. Figure S5: SEM-EDS mapping of catalyst Ir<sub>10.6</sub>@bpy-CTF400. Figure S6: Recyclability of Rh<sub>1.7</sub>@bpy-CTF400 and Ir<sub>4.7</sub>@bpy-CTF400. Figure S7: XPS of recovered Ir catalyst Ir<sub>4.7</sub>@bpy-CTF400. Table S1: Atomic composition of presented CTFs by SEM-EDS analysis. Table S2: N<sub>2</sub> adsorption-desorption analysis of prepared samples at 77K. Table S3. Elemental analysis of bpy-CTFs. Table S4: Base concentration vs Formate concentration at different intervals of time<sup>a</sup>.

**Author Contributions:** G.H.G., K.P. and H.J. performed experiments; G.H.G., K.-D.J. and S.Y. collected and analyzed data; K.P. and S.Y. computed density functional theory calculations; G.H.G. and S.Y. wrote the manuscript.

**Funding:** This research was funded by Korea CCS R&D Center (KCRC) grant funded by the Korea government (Ministry of Science, ICT & Future Planning) (No. 2014M1A8A1049300).

**Acknowledgments:** We acknowledge the financial support provided by the Korea CCS R&D Center (KCRC) grant funded by the Korea government (Ministry of Science, ICT & Future Planning) (no. 2014M1A8A1049300).

**Conflicts of Interest:** The authors declare no conflict of interest.

## References

1. Centi, G. Catalysis for CO<sub>2</sub> conversion: A key technology for rapid introduction of renewable energy in the value chain of chemical industries. *Energy Environ. Sci.* **2013**, *6*, 1711–1731. [[CrossRef](#)]
2. Klankermayer, J.; Wesselbaum, S.; Beydoun, K.; Leitner, W. Selective Catalytic Synthesis Using the Combination of Carbon Dioxide and Hydrogen: Catalytic Chess at the Interface of Energy and Chemistry. *Angew. Chem. Int. Ed.* **2016**, *55*, 7296–7343. [[CrossRef](#)] [[PubMed](#)]
3. Enthaler, S.; von Langermann, J.; Schmidt, T. Carbon dioxide and formic acid—The couple for environmental-friendly hydrogen storage? *Energy Environ. Sci.* **2010**, *3*, 1207–1217. [[CrossRef](#)]
4. Hull, J.F.; Hameda, Y.; Wang, W.-H.; Hashiguchi, B.; Periana, R.; Szalda, D.J.; Muckerman, J.T.; Fujita, E. Reversible hydrogen storage using CO<sub>2</sub> and a proton-switchable iridium catalyst in aqueous media under mild temperatures and pressures. *Nat. Chem.* **2012**, *4*, 383–388. [[CrossRef](#)] [[PubMed](#)]
5. Sudakar, P.; Sivanesan, D.; Yoon, S. Copolymerization of Epichlorohydrin and CO<sub>2</sub> Using Zinc Glutarate: An Additional Application of ZnGA in Polycarbonate Synthesis. *Macromol. Rapid Commun.* **2016**, *37*, 788–793. [[CrossRef](#)] [[PubMed](#)]
6. Sivanesan, D.; Kim, Y.E.; Youn, M.H.; Park, K.T.; Kim, H.-J.; Grace, A.N.; Jeong, S.K. The salt-based catalytic enhancement of CO<sub>2</sub> absorption by a tertiary amine medium. *RSC Adv.* **2016**, *6*, 64575–64580. [[CrossRef](#)]
7. Sivanesan, D.; Choi, Y.; Lee, J.; Youn, M.H.; Park, K.T.; Grace, A.N.; Kim, H.J.; Jeong, S.K. Carbon Dioxide Sequestration by Using a Model Carbonic Anhydrase Complex in Tertiary Amine Medium. *ChemSusChem* **2015**, *8*, 3977–3982. [[CrossRef](#)] [[PubMed](#)]
8. Sivanesan, D.; Youn, M.H.; Murnandari, A.; Kang, J.M.; Park, K.T.; Kim, H.J.; Jeong, S.K. Enhanced CO<sub>2</sub> absorption and desorption in a tertiary amine medium with a carbonic anhydrase mimic. *J. Ind. Eng. Chem.* **2017**, *52*, 287–294. [[CrossRef](#)]
9. Kieczska, H.; Reutemann, W. Formic acid. In *Ullmann's Encyclopedia of Industrial Chemistry*; Wiley: Hoboken, NJ, USA, 2002.
10. Grasemann, M.; Laurenczy, G. Formic acid as a hydrogen source—Recent developments and future trends. *Energy Environ. Sci.* **2012**, *5*, 8171–8181. [[CrossRef](#)]
11. Lau, C.P.; Chen, Y.Z. Hydrogenation of carbon dioxide to formic acid using a 6,6'-dichloro-2,2'-bipyridine complex of ruthenium, *cis*-[Ru(6,6'-Cl<sub>2</sub>bpy)<sub>2</sub>(H<sub>2</sub>O)<sub>2</sub>](CF<sub>3</sub>SO<sub>3</sub>)<sub>2</sub>. *J. Mol. Catal. A Chem.* **1995**, *101*, 33–36. [[CrossRef](#)]
12. Jessop, P.G.; Hsiao, Y.; Ikariya, T.; Noyori, R. Homogeneous catalysis in supercritical fluids: Hydrogenation of supercritical carbon dioxide to formic acid, alkyl formates, and formamides. *J. Am. Chem. Soc.* **1996**, *118*, 344–355. [[CrossRef](#)]
13. Gunasekar, G.H.; Yoon, Y.; Baek, I.; Yoon, S. Catalytic reactivity of an iridium complex with a proton responsive N-donor ligand in CO<sub>2</sub> hydrogenation to formate. *RSC Adv.* **2018**, *8*, 1346–1350. [[CrossRef](#)]

14. Wang, W.; Wang, S.; Ma, X.; Gong, J. Recent advances in catalytic hydrogenation of carbon dioxide. *Chem. Soc. Rev.* **2011**, *40*, 3703–3727. [[CrossRef](#)] [[PubMed](#)]
15. Schmeier, T.J.; Dobreiner, G.E.; Crabtree, R.H.; Hazari, N. Secondary coordination sphere interactions facilitate the insertion step in an iridium(III) CO<sub>2</sub> reduction catalyst. *J. Am. Chem. Soc.* **2011**, *133*, 9274–9277. [[CrossRef](#)] [[PubMed](#)]
16. Behr, A.; Nowakowski, K. *Catalytic Hydrogenation of Carbon Dioxide to Formic Acid*, 1st ed.; Elsevier Inc.: New York, NY, USA, 2014; Volume 66, ISBN 0898-8838.
17. Himeda, Y.; Onozawa-komatsuzaki, N.; Sugihara, H.; Kasuga, K. Simultaneous Tuning of Activity and Water Solubility of Complex Catalysts by Acid–Base Equilibrium of Ligands for Conversion of Carbon Dioxide. *Organometallics* **2007**, *26*, 702–712. [[CrossRef](#)]
18. Wang, W.H.; Himeda, Y.; Muckerman, J.T.; Manbeck, G.F.; Fujita, E. CO<sub>2</sub> Hydrogenation to Formate and Methanol as an Alternative to Photo- and Electrochemical CO<sub>2</sub> Reduction. *Chem. Rev.* **2015**, *115*, 12936–12973. [[CrossRef](#)] [[PubMed](#)]
19. Wang, W.-H.; Hull, J.F.; Muckerman, J.T.; Fujita, E.; Himeda, Y. Second-coordination-sphere and electronic effects enhance iridium(III)-catalyzed homogeneous hydrogenation of carbon dioxide in water near ambient temperature and pressure. *Energy Environ. Sci.* **2012**, *5*, 7923–7926. [[CrossRef](#)]
20. Maenaka, Y.; Suenobu, T.; Fukuzumi, S. Catalytic interconversion between hydrogen and formic acid at ambient temperature and pressure. *Energy Environ. Sci.* **2012**, *5*, 7360–7367. [[CrossRef](#)]
21. Gunasekar, G.H.; Park, K.; Jung, K.-D.; Yoon, S. Recent developments in the catalytic hydrogenation of CO<sub>2</sub> to formic acid/formate using heterogeneous catalysts. *Inorg. Chem. Front.* **2016**, *3*, 882–895. [[CrossRef](#)]
22. Stalder, C.J.; Chao, S.; Summers, D.P.; Wrighton, M.S. Supported Palladium Catalysts for the Reduction of Sodium Bicarbonate to Sodium Formate in Aqueous Solution at Room Temperature and One Atmosphere of Hydrogen. *J. Am. Chem. Soc.* **1983**, *105*, 6318–6320. [[CrossRef](#)]
23. Srivastava, V. Functionalized Hydrotalcite Tethered Ruthenium Catalyst for Carbon Sequestration Reaction. *Catal. Lett.* **2018**, *148*, 1879–1892. [[CrossRef](#)]
24. Zhang, Y.; Fei, J.; Yu, Y.; Zheng, X. Silica immobilized ruthenium catalyst used for carbon dioxide hydrogenation to formic acid (I): The effect of functionalizing group and additive on the catalyst performance. *Catal. Commun.* **2004**, *5*, 643–646. [[CrossRef](#)]
25. Wesselbaum, S.; Hintermair, U.; Leitner, W. Continuous-flow hydrogenation of carbon dioxide to pure formic acid using an integrated scCO<sub>2</sub> process with immobilized catalyst and base. *Angew. Chem. Int. Ed.* **2012**, *51*, 8585–8588. [[CrossRef](#)] [[PubMed](#)]
26. Xu, Z.; Mcnamara, N.D.; Neumann, G.T.; Schneider, W.F.; Hicks, J.C. Catalytic hydrogenation of CO<sub>2</sub> to formic acid with silica-tethered iridium catalysts. *ChemCatChem* **2013**, *5*, 1769–1771. [[CrossRef](#)]
27. McNamara, N.D.; Hicks, J.C. CO<sub>2</sub> capture and conversion with a multifunctional polyethyleneimine-tethered iminophosphine iridium catalyst/adsorbent. *ChemSusChem* **2014**, *7*, 1114–1124. [[CrossRef](#)] [[PubMed](#)]
28. Gunasekar, G.H.; Shin, J.; Jung, K.-D.; Park, K.; Yoon, S. Design Strategy Toward Recyclable and Highly Efficient Heterogeneous Catalysts for the Hydrogenation of CO<sub>2</sub> to Formate. *ACS Catal.* **2018**, *8*, 4346–4353. [[CrossRef](#)]
29. Park, K.; Gunasekar, G.H.; Prakash, N.; Jung, K.-D.; Yoon, S. A Highly Efficient Heterogenized Iridium Complex for the Catalytic Hydrogenation of Carbon Dioxide to Formate. *ChemSusChem* **2015**, *8*, 3410–3413. [[CrossRef](#)] [[PubMed](#)]
30. Bavykina, A.V.; Rozhko, E.; Goesten, M.G.; Wezendonk, T.; Seoane, B.; Kapteijn, F.; Makkee, M.; Gascon, J. Shaping Covalent Triazine Frameworks for the Hydrogenation of Carbon Dioxide to Formic Acid. *ChemCatChem* **2016**, *8*, 2217–2221. [[CrossRef](#)]
31. Gunniya Hariyanandam, G.; Hyun, D.; Natarajan, P.; Jung, K.D.; Yoon, S. An effective heterogeneous Ir(III) catalyst, immobilized on a heptazine-based organic framework, for the hydrogenation of CO<sub>2</sub> to formate. *Catal. Today* **2016**, *265*, 52–55. [[CrossRef](#)]
32. Gunasekar, G.H.; Park, K.; Ganesan, V.; Lee, K.; Kim, N.K.; Jung, K.D.; Yoon, S. A Covalent Triazine Framework, Functionalized with Ir/N-Heterocyclic Carbene Sites, for the Efficient Hydrogenation of CO<sub>2</sub> to Formate. *Chem. Mater.* **2017**, *29*, 6740–6748. [[CrossRef](#)]
33. Preti, D.; Resta, C.; Squarzialupi, S.; Fachinetti, G. Carbon dioxide hydrogenation to formic acid by using a heterogeneous gold catalyst. *Angew. Chem. Int. Ed.* **2011**, *50*, 12551–12554. [[CrossRef](#)] [[PubMed](#)]

34. Bi, Q.Y.; Lin, J.D.; Liu, Y.M.; Du, X.L.; Wang, J.Q.; He, H.Y.; Cao, Y. An aqueous rechargeable formate-based hydrogen battery driven by heterogeneous Pd catalysis. *Angew. Chem. Int. Ed.* **2014**, *53*, 13583–13587. [[CrossRef](#)] [[PubMed](#)]
35. Su, J.; Lu, M.; Lin, H. High yield production of formate by hydrogenating CO<sub>2</sub> derived ammonium carbamate/carbonate at room temperature. *Green Chem.* **2015**, *17*, 2769–2773. [[CrossRef](#)]
36. Nguyen, L.T.M.; Park, H.; Banu, M.; Kim, J.Y.; Youn, D.H.; Magesh, G.; Kim, W.Y.; Lee, J.S. Catalytic CO<sub>2</sub> hydrogenation to formic acid over carbon nanotube-graphene supported PdNi alloy catalysts. *RSC Adv.* **2015**, *5*, 105560–105566. [[CrossRef](#)]
37. Filonenko, G.A.; Vrijburg, W.L.; Hensen, E.J.M.; Pidko, E.A. On the activity of supported Au catalysts in the liquid phase hydrogenation of CO<sub>2</sub> to formates. *J. Catal.* **2016**, *343*, 97–105. [[CrossRef](#)]
38. Umegaki, T.; Enomoto, Y.; Kojima, Y. Metallic ruthenium nanoparticles for hydrogenation of supercritical carbon dioxide. *Catal. Sci. Technol.* **2016**, *6*, 409–412. [[CrossRef](#)]
39. Wang, T.; Ren, D.; Huo, Z.; Song, Z.; Jin, F.; Chen, M.; Chen, L. A nanoporous nickel catalyst for selective hydrogenation of carbonates into formic acid in water. *Green Chem.* **2017**, *19*, 716–721. [[CrossRef](#)]
40. Patel, P.; Nandi, S.; Maru, M.S.; Kureshy, R.I.; Khan, N.U.H. Nitrogen-rich graphitic carbon stabilized cobalt nanoparticles as an effective heterogeneous catalyst for hydrogenation of CO<sub>2</sub> to formate. *J. CO<sub>2</sub> Util.* **2018**, *25*, 310–314. [[CrossRef](#)]
41. Jiang, J.; Gunasekar, G.H.; Park, S.; Kim, S.-H.; Yoon, S.; Piao, L. Hierarchical Cu nanoparticle-aggregated cages with high catalytic activity for reduction of 4-nitrophenol and carbon dioxide. *Mater. Res. Bull.* **2018**, *100*, 184–190. [[CrossRef](#)]
42. Maru, M.S.; Ram, S.; Adwani, J.H.; Shukla, R.S. Selective and Direct Hydrogenation of CO<sub>2</sub> for the Synthesis of Formic Acid over a Rhodium Hydrotalcite (Rh-HT) Catalyst. *ChemistrySelect* **2017**, *2*, 3823–3830. [[CrossRef](#)]
43. Yang, Z.-Z.; Zhang, H.; Yu, B.; Zhao, Y.; Ji, G.; Liu, Z. A Tröger's base-derived microporous organic polymer: Design and applications in CO<sub>2</sub>/H<sub>2</sub> capture and hydrogenation of CO<sub>2</sub> to formic acid. *Chem. Commun.* **2015**, *51*, 1271–1274. [[CrossRef](#)] [[PubMed](#)]
44. Kann, A.; Hartmann, H.; Besmehn, A.; Hausoul, P.; Palkovits, R. Hydrogenation of CO<sub>2</sub> to Formate over Ru Immobilized on Solid Molecular Phosphines. *ChemSusChem* **2018**, *11*, 1857–1865. [[CrossRef](#)] [[PubMed](#)]
45. Bavykina, A.V.; Olivos-Suarez, A.I.; Osadchii, D.; Valecha, R.; Franz, R.; Makkee, M.; Kapteijn, F.; Gascon, J. Facile Method for the Preparation of Covalent Triazine Framework coated Monoliths as Catalyst Support: Applications in C1 Catalysis. *ACS Appl. Mater. Interfaces* **2017**, *9*, 26060–26065. [[CrossRef](#)] [[PubMed](#)]
46. Rajendiran, S.; Gunasekar, G.H.; Yoon, S. A heterogenized cobaltate catalyst on a bis-imidazolium-based covalent triazine framework for hydroesterification of epoxides. *New J. Chem.* **2018**, *42*, 12256–12262. [[CrossRef](#)]
47. Hao, L.; Ning, J.; Luo, B.; Wang, B.; Zhang, Y.; Tang, Z.; Yang, J.; Thomas, A.; Zhi, L. Structural evolution of 2D microporous covalent triazine-based framework toward the study of high-performance supercapacitors. *J. Am. Chem. Soc.* **2015**, *137*, 219–225. [[CrossRef](#)] [[PubMed](#)]
48. Puthiaraj, P.; Lee, Y.-R.; Zhang, S.; Ahn, W.-S. Triazine-based covalent organic polymers: Design, synthesis and applications in heterogeneous catalysis. *J. Mater. Chem. A* **2016**, *4*, 16288–16311. [[CrossRef](#)]
49. Rajendiran, S.; Natarajan, P.; Yoon, S. A covalent triazine framework-based heterogenized Al-Co bimetallic catalyst for the ring-expansion carbonylation of epoxide to beta-lactone. *RSC Adv.* **2017**, *7*, 4635–4638. [[CrossRef](#)]
50. Park, K.; Lee, K.; Kim, H.; Ganesan, V.; Cho, K.; Jeong, S.K.; Yoon, S. Preparation of covalent triazine frameworks with imidazolium cations embedded in basic sites and their application for CO<sub>2</sub> capture. *J. Mater. Chem. A* **2017**, *5*, 8576–8582. [[CrossRef](#)]
51. Puthiaraj, P.; Kim, S.S.; Ahn, W.S. Covalent triazine polymers using a cyanuric chloride precursor via Friedel-Crafts reaction for CO<sub>2</sub> adsorption/separation. *Chem. Eng. J.* **2016**, *283*, 184–192. [[CrossRef](#)]
52. Kuhn, P.; Forget, A.; Su, D.; Thomas, A.; Antonietti, M. From microporous regular frameworks to mesoporous materials with ultrahigh surface area: Dynamic reorganization of porous polymer networks. *J. Am. Chem. Soc.* **2008**, *130*, 13333–13337. [[CrossRef](#)] [[PubMed](#)]
53. Kuhn, P.; Antonietti, M.; Thomas, A. Porous, covalent triazine-based frameworks prepared by ionothermal synthesis. *Angew. Chem. Int. Ed.* **2008**, *47*, 3450–3453. [[CrossRef](#)] [[PubMed](#)]
54. Kuhn, P.; Thomas, A.; Antonietti, M. Toward tailorable porous organic polymer networks: A high-temperature dynamic polymerization scheme based on aromatic nitriles. *Macromolecules* **2009**, *42*, 319–326. [[CrossRef](#)]

55. Palkovits, R.; Antonietti, M.; Kuhn, P.; Thomas, A.; Schüth, F. Solid catalysts for the selective low-temperature oxidation of methane to methanol. *Angew. Chem. Int. Ed.* **2009**, *48*, 6909–6912. [[CrossRef](#)] [[PubMed](#)]
56. Kuhn, P.; Forget, A.; Hartmann, J.; Thomas, A.; Antonietti, M. Template-free tuning of nanopores in carbonaceous polymers through ionothermal synthesis. *Adv. Mater.* **2009**, *21*, 897–901. [[CrossRef](#)]
57. Palkovits, R.; von Malotki, C.; Baumgarten, M.; Müllen, K.; Baltes, C.; Antonietti, M.; Kuhn, P.; Weber, J.; Thomas, A.; Schüth, F. Development of molecular and solid catalysts for the direct low-temperature oxidation of methane to methanol. *ChemSusChem* **2010**, *3*, 277–282. [[CrossRef](#)] [[PubMed](#)]
58. Hug, S.; Tauchert, M.E.; Li, S.; Pachmayr, U.E.; Lotsch, B.V. A functional triazine framework based on N-heterocyclic building blocks. *J. Mater. Chem.* **2012**, *22*, 13956–13964. [[CrossRef](#)]
59. Hug, S.; Stegbauer, L.; Oh, H.; Hirscher, M.; Lotsch, B.V. Nitrogen-Rich Covalent Triazine Frameworks as High-Performance Platforms for Selective Carbon Capture and Storage. *Chem. Mater.* **2015**, *27*, 8001–8010. [[CrossRef](#)]
60. Rajendiran, S.; Park, K.; Lee, K.; Yoon, S. Ionic-Liquid-Based Heterogeneous Covalent Triazine Framework Cobalt Catalyst for the Direct Synthesis of Methyl 3-Hydroxybutyrate from Propylene Oxide. *Inorg. Chem.* **2017**, *56*, 7270–7277. [[CrossRef](#)] [[PubMed](#)]
61. Sudakar, P.; Gunasekar, G.H.; Baek, I.H.; Yoon, S. Recyclable and efficient heterogenized Rh and Ir catalysts for the transfer hydrogenation of carbonyl compounds in aqueous medium. *Green Chem.* **2016**, *18*, 6456–6461. [[CrossRef](#)]
62. Bavykina, A.V.; Goesten, M.G.; Kapteijn, F.; Makkee, M.; Gascon, J. Efficient production of hydrogen from formic acid using a Covalent Triazine Framework supported molecular catalyst. *ChemSusChem* **2015**, *8*, 809–812. [[CrossRef](#)] [[PubMed](#)]
63. Park, K.; Lim, S.; Baik, J.H.; Kim, H.; Jung, K.-D.; Yoon, S. Exceptionally Stable Rh-based Molecular Catalyst Heterogenized on a Cationically charged Covalent Triazine Framework Support for Efficient Methanol Carbonylation. *Catal. Sci. Technol.* **2018**, *8*, 2894–2900. [[CrossRef](#)]
64. Jena, H.S.; Krishnaraj, C.; Wang, G.; Leus, K.; Schmidt, J.; Chaoui, N.; Van Der Voort, P. Acetylacetone Covalent Triazine Framework: An Efficient Carbon Capture and Storage Material and a Highly Stable Heterogeneous Catalyst. *Chem. Mater.* **2018**, *30*, 4102–4111. [[CrossRef](#)]
65. Sharifi, T.; Gracia-Espino, E.; Reza Barzegar, H.; Jia, X.; Nitze, F.; Hu, G.; Nordblad, P.; Tai, C.W.; Wågberg, T. Formation of nitrogen-doped graphene nanoscrolls by adsorption of magnetic  $\gamma$ -Fe<sub>2</sub>O<sub>3</sub> nanoparticles. *Nat. Commun.* **2013**, *4*, 2319. [[CrossRef](#)] [[PubMed](#)]
66. Chan-Thaw, C.E.; Villa, A.; Katekomol, P.; Su, D.; Thomas, A.; Prati, L. Covalent triazine framework as catalytic support for liquid phase reaction. *Nano Lett.* **2010**, *10*, 537–541. [[CrossRef](#)] [[PubMed](#)]
67. Himeda, Y. Conversion of CO<sub>2</sub> into formate by homogeneously catalyzed hydrogenation in water: Tuning catalytic activity and water solubility through the acid-base equilibrium of the ligand. *Eur. J. Inorg. Chem.* **2007**, *2007*, 3927–3941. [[CrossRef](#)]
68. Balcells, D.; Nova, A.; Clot, E.; Gnanamgari, D.; Crabtree, R.H.; Eisenstein, O. Mechanism of homogeneous iridium-catalyzed alkylation of amines with alcohols from a DFT study. *Organometallics* **2008**, *27*, 2529–2535. [[CrossRef](#)]
69. Bartoszewicz, A.; González Miera, G.; Marcos, R.; Norrby, P.O.; Martín-Matute, B. Mechanistic studies on the alkylation of amines with alcohols catalyzed by a bifunctional iridium complex. *ACS Catal.* **2015**, *5*, 3704–3716. [[CrossRef](#)]
70. Ertem, M.Z.; Himeda, Y.; Fujita, E.; Muckerman, J.T. Interconversion of Formic Acid and Carbon Dioxide by Proton-Responsive, Half-Sandwich CpIrIII Complexes: A Computational Mechanistic Investigation. *ACS Catal.* **2016**, *6*, 600–609. [[CrossRef](#)]
71. Suna, Y.; Ertem, M.Z.; Wang, W.; Kambayashi, H.; Manaka, Y.; Muckerman, J.T.; Fujita, E.; Himeda, Y. Positional Effects of Hydroxy Groups on Catalytic Activity of Proton-Responsive Half-Sandwich Cp\*Iridium(III) Complexes. *Organometallics* **2014**, *33*, 6519–6530. [[CrossRef](#)]

